Engineering Failure Analysis 149 (2023) 107285

Contents lists available at ScienceDirect

Engineering Failure Analysis

journal homepage: www.elsevier.com/locate/engfailanal

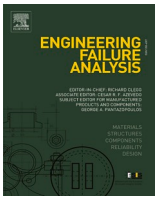

Fractographic-fractal dimension correlation with crack initiation and fatigue life for notched aluminium alloys under bending load

Wojciech Macek [a,*], Dariusz Rozumek [b], Sebastian Faszynka [b], Ricardo Branco [c], Shun-Peng Zhu [d], Reza Masoudi Nejad [d]

[a] Gdańsk University of Technology, Faculty of Mechanical Engineering and Ship Technology, Gdańsk, Poland
[b] Opole University of Technology, Faculty of Mechanical Engineering, Opole, Poland
[c] University of Coimbra, CEMMPRE, Department of Mechanical Engineering, Coimbra, Portugal
[d] School of Mechanical and Electrical Engineering, University of Electronic Science and Technology of China, Chengdu 611731, China

ARTICLE INFO

Keywords:
Fractography
Fractal dimension
Aluminium alloy
Bending fatigue
Fatigue crack initiation
Fatigue life estimation
Entire fracture surface method

ABSTRACT

In this study, fatigue fracture surfaces of aluminium alloy 2017-T4 notched specimens were investigated under cyclic bending to find an alternative failure loading index.. The surface topographies were measured on the entire fracture area with an optical profilometer for different loading conditions. Fatigue crack initiation life N_i and total fatigue life N_f were examined using standard surface topography parameters (such as, root mean square height *Sq*, arithmetical mean height *Sa*, maximum height *Sz*) and non-standard surface topography parameters (such as, fractal dimension D_f). Fatigue life assessment was successfully performed by combining both fracture surface topography and stress state features. The results show that the fracture plane geometry, expressed by the fractographic-fractal dimension, can facilitate the estimation of post-failure loading history.

1. Introduction

Aluminium alloys have a favorable strength-to-weight ratio, when compared to steel, which makes them attractive for critical structural applications [1,2]. Hard aluminum alloy 2017, which was considered in this work, has been extensively used in aeronautics and astronautics [3]. In these fields, a significant number of decisive elements experience multiaxial loading [4], bending loading [5] or creep at elevated temperature [6] increasing the risk of fatigue failure. Manufacturing processes and joining technology of aluminium alloy components can also affect the fatigue lifetime and, thus, its durability and degree of safety [7–9].

The geometry and shape of structural elements, e.g. thin-walled structures [10], or notched structures [11], are other important factors in the context of fatigue design. The understanding of geometry and shape features on mechanical behaviour requires not only efficient manufacturing processes and optimized topological configurations, but also the development of reliable predictive models [12]. Marciniak et al. [13] studied the influence of defect features on fatigue behaviour in structural steel subjected to bending and torsion. An interesting outcome was that fatigue performance is significantly affected by both the defect orientation and the defect shape. Deng et al. [14] proposed a new method to account for the degree of non-proportionality under complex multiaxial loading histories based on equivalent strain damage parameter computed at the critical plane.

The fatigue life of critical elements is often defined as the number of cycles needed to initiate a fatigue crack or the number of cycles

* Corresponding author.
E-mail address: wojciech.macek@pg.edu.pl (W. Macek).

https://doi.org/10.1016/j.engfailanal.2023.107285
Received 15 January 2023; Received in revised form 20 February 2023; Accepted 24 April 2023
Available online 29 April 2023

Nomenclature

a	crack size [mm]
b	cross-section width [mm]
D_f	fractal dimension [–]
E	Young's modulus [GPa]
h	cross-section height [Mm]
K'	cyclic hardening coefficient [MPa]
K_t	theoretical stress concentration factor [–]
M_B	bending moment [Nm]
N_i	number of cycles to crack initiation [Cycles]
N_{ical}	predicted number of cycles to crack initiation [cycles]
N_f	number of cycles to failure [Cycles]
N_{fcal}	predicted number of cycles to failure [Cycles]
n'	cyclic hardening exponent [–]
P	topographic stress factor [MPa]
R	stress ratio [–]
R^2	coefficient of determination [–]
Ra	arithmetical mean height (profile) [μm]
Sa	arithmetical mean height [Mm]
Sq	root mean square height [mm]
Sz	maximum height [Mm]
V	surface volume (for fractal dimension calculation) [μm^3]
Vmc	core material volume [mm^3/mm^2]
Vmp	peak material volume [mm^3/mm^2]
Vv	void volume [mm^3/mm^2]
Vvc	core void volume [mm^3/mm^2]
Vvv	pit void volume [mm^3/mm^2]
ε	width (for fractal dimension calculation) [Mm]
σ_Y	yield strength [MPa]
σ_{US}	tensile strength [MPa]
υ	Poisson's ratio [-]
σ_a	nominal normal stress amplitude [MPa]
σ_{max}	maximum normal stress [MPa]

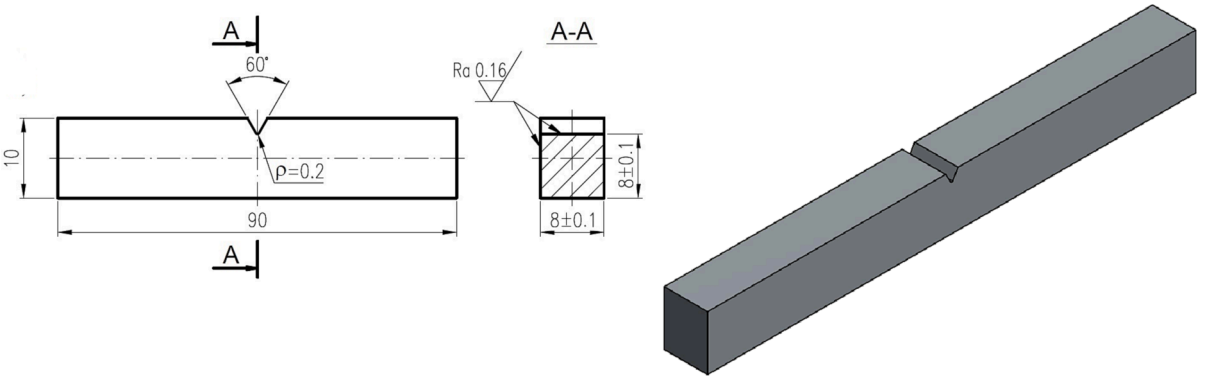

Fig. 1. Geometry of the notched specimen (dimensions in millimeters).

Table 1
Composition of a substance of the 2017A-T4 (wt.%) [1].

Material	Cu	Mn	Zn	Mg	Fe	Cr	Si	Ti	Al
2017A-T4	4.15	0.65	0.50	0.69	0.70	0.10	0.45	0.20	Bal.

Table 2
Monotonic quasi-static tension properties of the 2017A-T4 [1].

Material	σ_y (MPa)	σ_{us} (MPa)	E (GPa)	ν (–)
2017A-T4	382	480	72	0.32

Table 3
Loading scenarios of the tested specimens [37].

Specimen	σ_{max} (MPa)	R
S1	698	0
S2	349	0
S3	698	−0.5
S4	698	−1
S5	698	−1
S6	349	−0.5
S7	349	−1

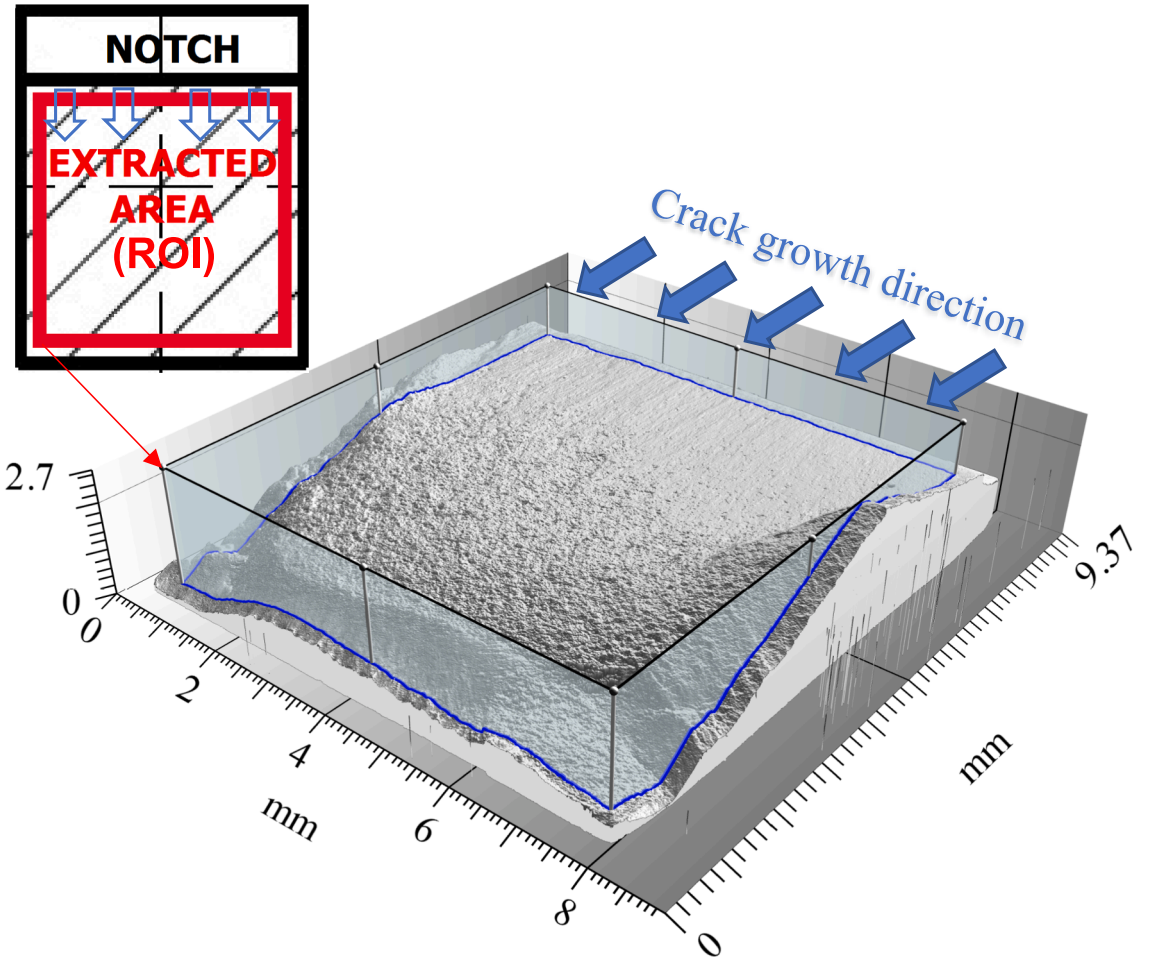

Fig. 2. Scheme of the extracted area – Region of Interest (ROI).

needed to growth a crack from an initial length to a pre-defined value. Thus, the design of such elements is carried out to ensure that the crack develops slowly, in detectable locations, allowing regular inspection and maintenance tasks [15]. Modern design is generally supported by numerical methods, like the finite element method [16] and is grounded on physically-based interpretations established on the basis of fracture energy concepts [17]. Due to the complexity of real service conditions, fatigue crack growth rates are

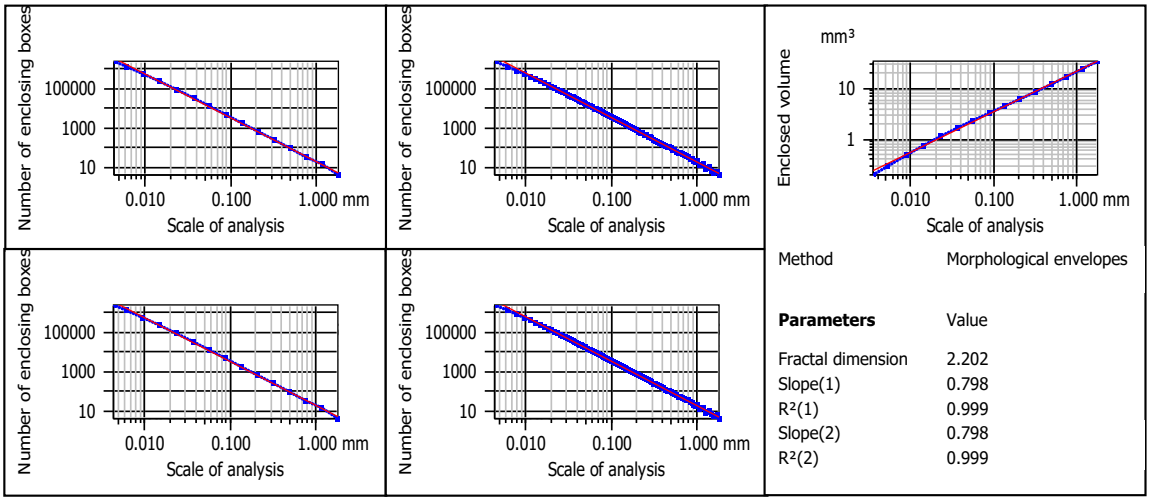

Fig. 3. Fractal analysis for the extracted area using the entire fracture surface method: (a) enclosing boxes – coarse resolution; (b) enclosing boxes – extra-fine resolution; (c) morphological envelopes - coarse resolution; (d) enclosing boxes in real units – coarse resolution; and (e) enclosing boxes in real units – extra-fine resolution.

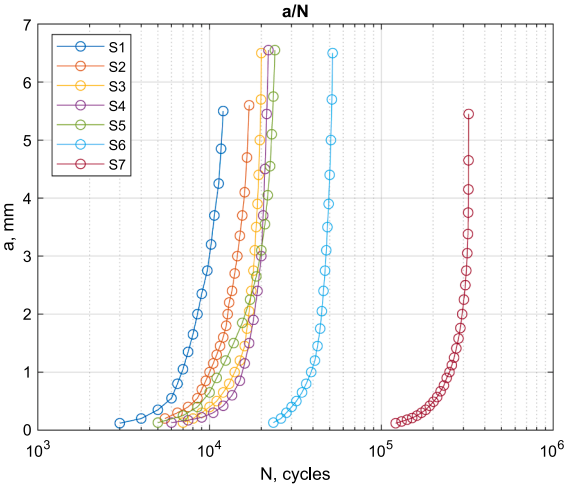

Fig. 4. Fatigue crack propagation curves.

Table 4
Fatigue lives determined from the experimental a-N curves [37].

Specimen	N_i (cycles)	N_f (cycles)
S1	3×10^3	12×10^3
S2	5.5×10^3	17×10^3
S3	7×10^3	20×10^3
S4	6×10^3	22×10^3
S5	5×10^3	24×10^3
S6	23.5×10^3	52×10^3
S7	121×10^3	322×10^3

investigated not only under mode-I but also under mixed-mode loading [18].

Surface topography is an important indicator of fractured surface integrity assessment [19]. It can provide valuable information about the loading history of the post-mortem inspected elements [20]. In most cases, fracture surfaces obtained in fatigue tests are so complex and their description is carried out not only using height *Sx* or volumetric *Vx* parameters, but also using other parameters not covered in the standards [21,22], such as fractal dimension D_f [23,24]. Some attention has been put on fractal dimension sensitivity for different fracture mechanisms [25]. In general, average values of fractal dimension, irrespective of the tested material (aluminium or

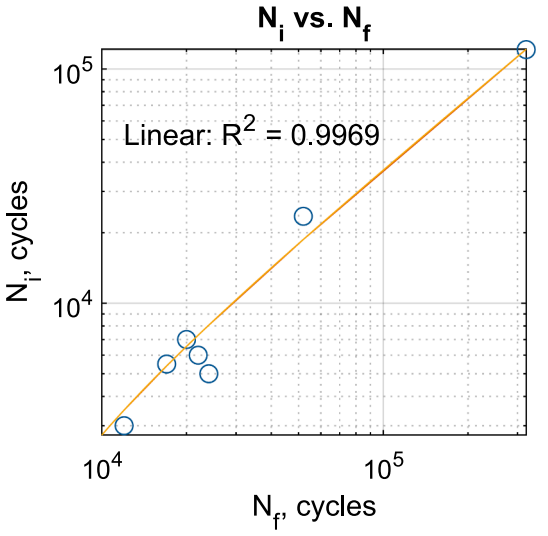

Fig. 5. Fatigue crack initiation life N_i versus total fatigue life N_f.

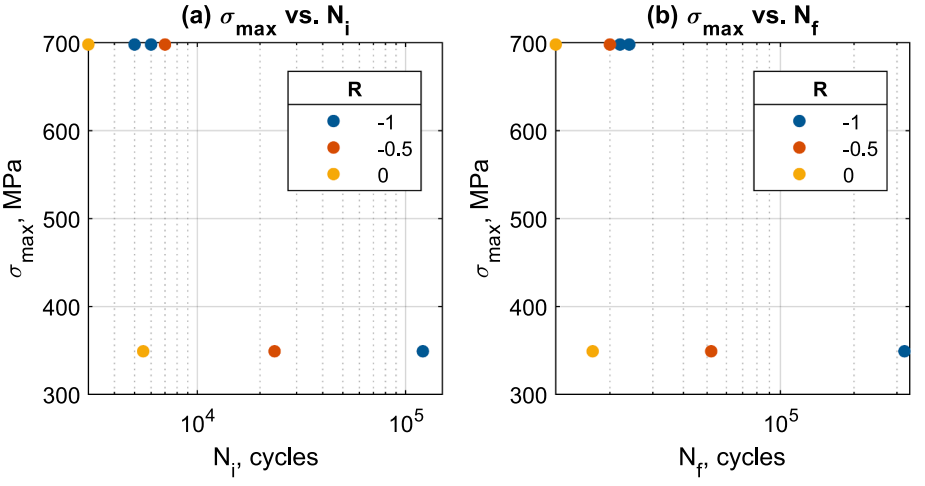

Fig. 6. Maximum normal stress σ_{max} versus experimental fatigue life: (a) N_i; (b) N_f.

steel alloys) were higher for bending, while the minimum values were found for bending–torsion. The analysis of fracture surfaces has also found application to explain different fatigue phenomena [26–29] and, especially, in the context of fractal dimension [30,31]. Konate et al. [30] showed the scale invariant properties of cracks in 2D elastic materials with disordered fracture properties. They concluded that Displacement Discontinuity Method allows for a fast calculation of crack profiles over sufficiently long distances. They proposed an methodology for the observation of two different types of fracture morphologies in 2D disordered brittle solids. In another paper, Berthier et al. [31] investigated both numerically and theoretically the initial phase of damage accumulation prior to failure in quasi-brittle solids. They predicted the catastrophic failure, including its location, and were able to capture qualitatively the main features of the rugged evolution of damage observed experimentally in quasi-brittle solids under compression.

In addition to 3D quantitative fractography of fatigue fractures, qualitative methods of recreating cracking mechanisms such as FRASTA are also used [32–34]. Therefore, modern 3D fractography requires the advanced methods and reliable tools for measuring surface topography [35,36].

This work aims primarily to investigate the sensitivity of fractographic-fractal dimension to deal with crack initiation and fatigue durability problems in notched aluminium alloys subjected to cyclic bending [37]. It is also unclear how the different approaches of determining the fractal dimension [38], via the entire fracture surface method [39], can influence the correlation between the fractographic features and the fractal dimension. In order to address these goals, it is pivotal to identify the relevant parameters in terms loading history, description of fatigue cracking process and fatigue life assessment, based on the metrology of the fracture surfaces.

These goals include several innovative aspects: (1) the link between the fracture surface with loading type using adequate fractographic parameters; (2) the identification of feasible methods for fatigue life assessment and feasible parameters for the

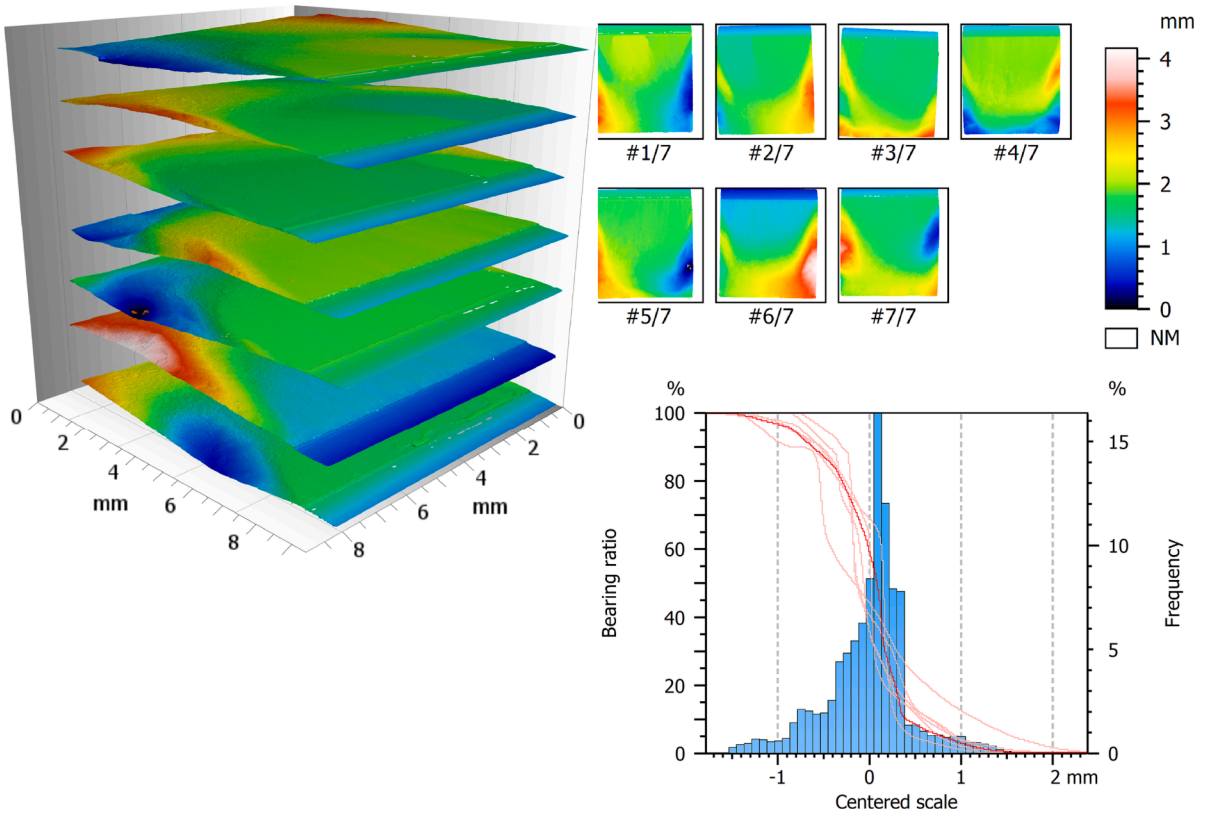

Fig. 7. Measured fractures in the form of 3D and grid views with histogram and Abbott-Firestone curves.

characterization of the cracking process; and (3) the understanding of fracture mechanisms for notched aluminium alloys under various loading conditions.

2. Methodology

2.1. Material and specimens

This research has been conducted on V-notched rectangular cross-section beams made of AW-2017A-T4 aluminium alloy (see Fig. 1). The material details regarding the chemical composition and monotonic quasi-static tensile properties are presented in Tables 1 and 2, respectively [1]. The specimen geometry with one-side notch (depth of 2 mm, notch angle of 60°, and notch radius of 0.2 mm) was obtained from a rod with a diameter of 16 mm.

2.2. Bending fatigue tests

The bending fatigue tests were performed for three stress ratios ($R = \sigma_{min}/\sigma_{max} = -1, -0.5$, and 0) and two maximum normal stress (σ_{max}) levels. Details about the loading cases are summarized in Table 3. The theoretical stress concentration factor evaluated by analytical calculations from [40] for bending is $K_t = 3.76$. The maximum normal stress at the notch root (σ_{max}) can be defined using the following relationship:

$$\sigma_{max} = \sigma_a K_t \tag{1}$$

where σ_a is nominal normal stress amplitude determined from the formula:

$$\sigma_a = \frac{6M_B}{bh^2} \tag{2}$$

where M_B is the bending moment, b is the width, and h is the height of the cross-section.

A portable microscope with a constant magnification of 25 × with a micrometer accuracy of $\Delta a = 0.01$ mm was used to measure the crack length during the tests and the associated number of loading cycles. The experimental fatigue lives were determined from a-N curves, i.e. curves relating the crack length with the number of loading cycles. The crack length corresponds to lateral surface crack

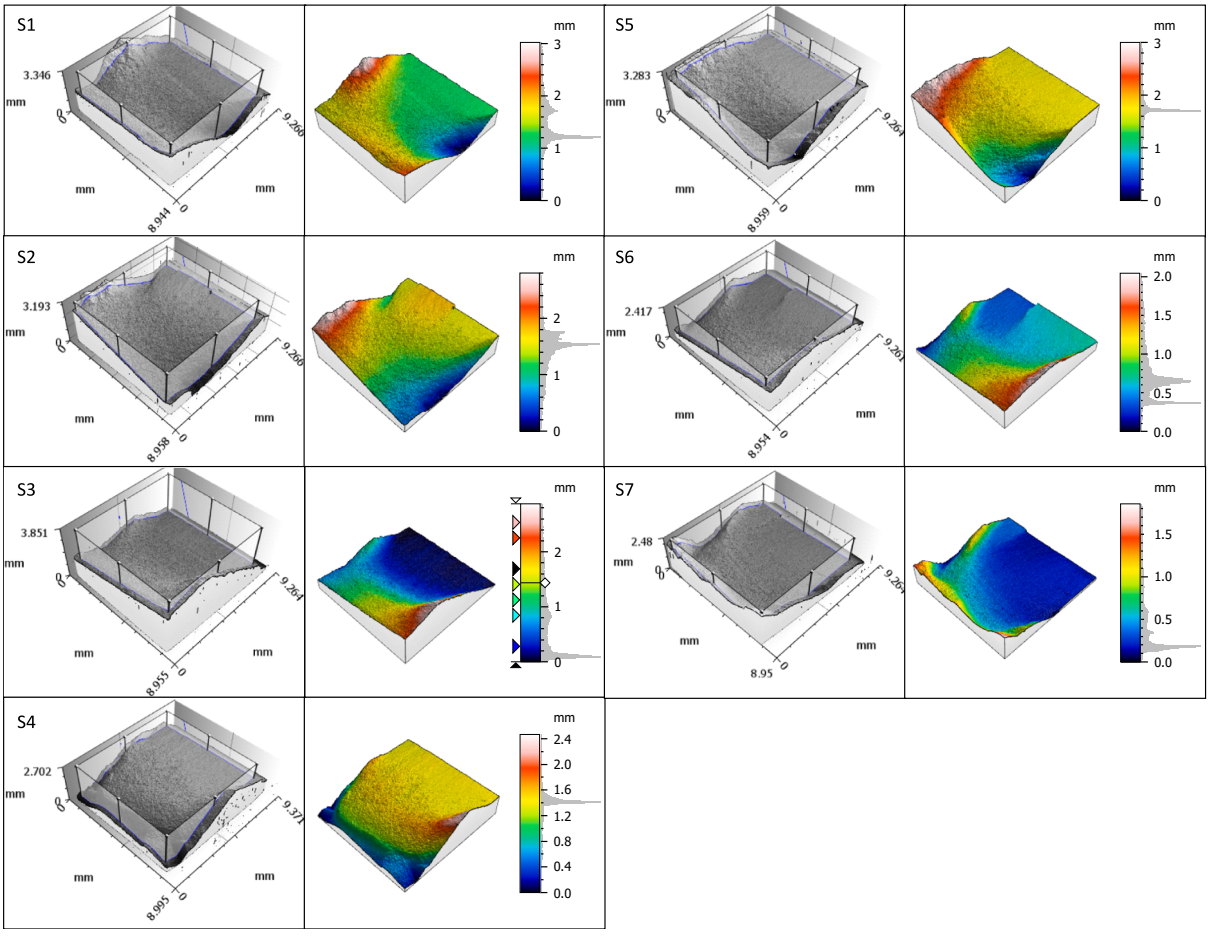

Fig. 8. Extracted surfaces of fractures for the region of interest (ROI).

length a measured from the active side of the specimen. The number of cycles to fatigue crack initiation N_i was defined for lateral crack size a equal to 0.12 mm.

2.3. *Fracture surface investigation*

It is recommended to use various measurement methods and scales of analysis in the study of the shape of fracture surfaces. In this way, it is possible to obtain complete information on fracture formation and failure mechanisms. However, the assumption of the entire fracture surface method is the quantitative assessment of surface on a macro scale.

The 3D profilometer used in this work is an Alicona Infinite Focus G4 equipped with a 10 × objective which ensures a higher field of view. The vertical resolution measurement was about 80 nm and the lateral resolution estimate to 3.9 μm. Using the ImageField function, the entire fracture surface can be captured with 9 rows and 7 columns merged in one image. MountainsMap surface topography software was used to analyse and visualization of fractures. The whole surface was reduced to eliminate the regions associated with the geometric discontinuities and to obtain uniform dimensions for all bending specimens, as shown in Fig. 2. The surface was limited to a rectangular area with 7.2 mm × 7.5 mm. According to the entire fracture surface method, used in this study, the same criterium was applied to all extracted areas. The blue arrows indicate the crack growth direction that initiated from the notch root under bending in all cases.

The examined surfaces were analised by computing the fractal dimension D_f. In this approach, when the surface is divided, algorithms must maintain the number of iterations that take place. The resolution of the plot decides both the number of iterations and the calculation time. In this analysis, for coarse resolution, it was used 15 data points, and for extra-fine resolution, it was used 96 data points. The Enclosing Boxes Method (EBM) divides the area into smaller divisions with a width ε and calculates the volume ($V\varepsilon$) of all volumes covering the entire area. This is an iterative procedure where the width of the box is changed to plot in the form $\ln(V\varepsilon)/\ln(\varepsilon)$. A logarithmic scale is used for the axes, but the values of the divisions are given as dimensional units. To estimate the fractal dimension D_f, a line is fitted using the least square method. The absolute value of the slope of the fitted line is the valuation of the fractal dimension D_f.

Table 5
Summary of the *Sx* and *Vx* results.

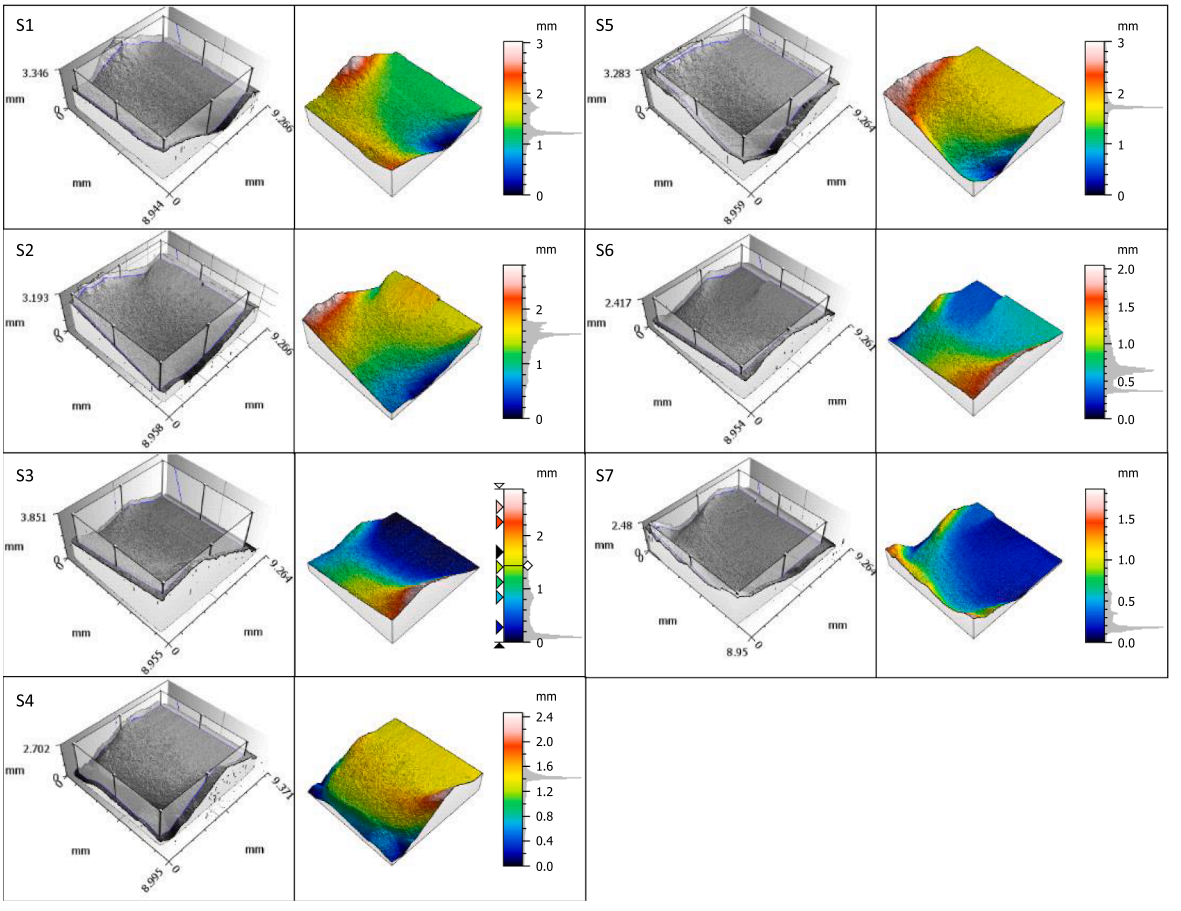

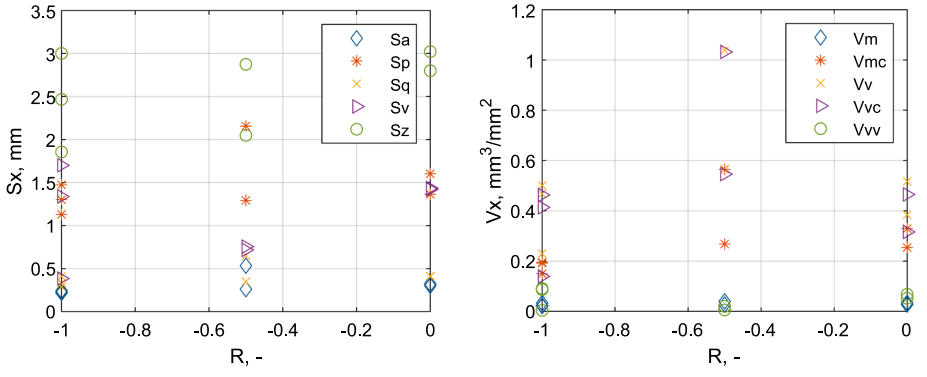

Fig. 9. Surface parameters *Sx* and *Vx* versus stress ratio, *R*: (a) *Sx*; (b) *Vx*.

Fig. 3 shows exemplary plots of fractal dimension determined for coarse resolution and extra-fine resolution. The curve is shown in blue while the regression line is plotted in red. The morphological envelopes method (see Fig. 3(c)) embraces the upper and lower envelopes, which are calculated by morphological opening and closing, interposing a structuring element that is a horizontal line segment of length ε. The computed volume for surfaces ($V\varepsilon$) is plotted as a function of the scale $\ln(V\varepsilon)/\ln(\varepsilon)$. The fractal dimension D_f is calculated from the slope of one of the two regression lines that best fits the data. In box counting, the real scale and unit are unknown, so the surface is sampled using arbitrary values of *V* and the unit of detail is deduced from the data after the calculation. The enclosing boxes for the real unit method (see Fig. 3(d,e)) is similar to EBM, but it uses boxes with a width in real size, instead of a width in points.

The surface characterization also included a texture isotropy study which aimed to calculate the isotropy parameters with respect to

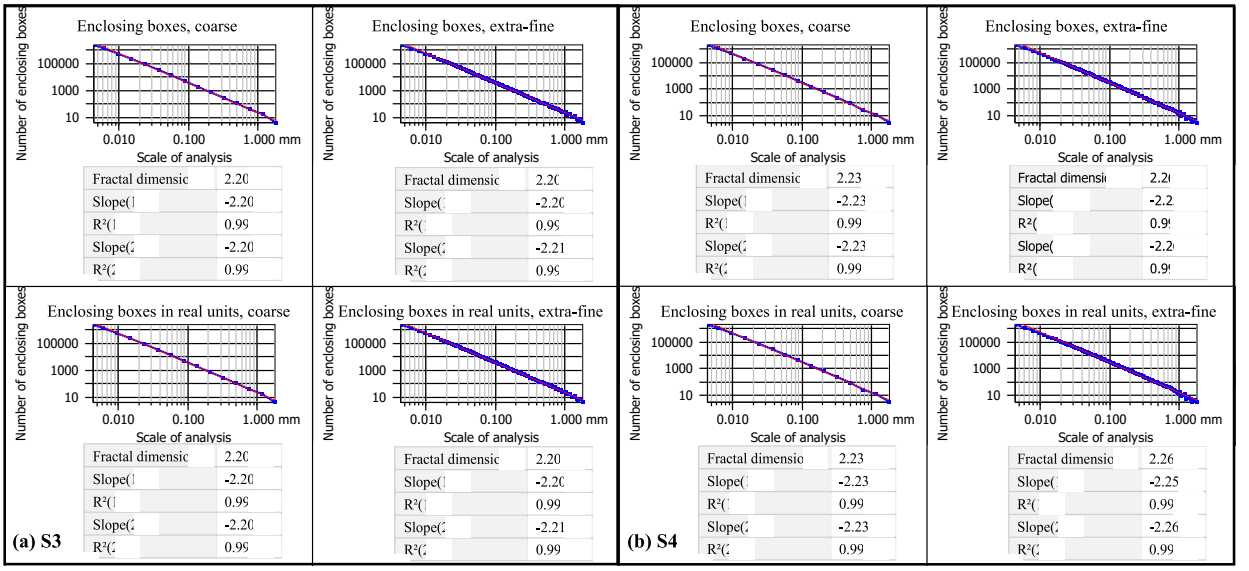

Fig. 10. Extreme fractal dimension D_f results: (a) S3 – minimum, and (b) S4 – maximum.

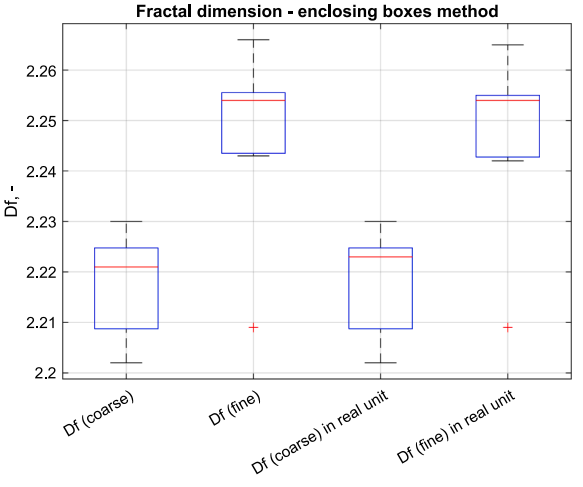

Fig. 11. Boxplot for fractal dimension D_f grouped by EBM calculations parameters.

a user-defined threshold, assumed here equal to 0.20. These values allowed to quantify the central zones corresponding to the portion of the peaks that remained after thresholding.

3. Results

3.1. Crack growth and bending fatigue tests

Thanks to mapping the entire crack propagation characteristics, crack propagation curves provide beneficial information on the critical fracture indices for the tested material. Such data include information from the instant of crack detection to the threshold value of crack at the unstable crack growth and final rupture stage. The crack propagation curves, i.e the so-called *a-N* curves, for different loading cases are shown in Fig. 4 [37]. The results of both the fatigue crack initiation N_i and the total fatigue life N_f are shown in Table 4. As mentioned above, the crack initiation was defined based on the lateral crack size for a length of 0.12 mm.

Fig. 5 shows the mutual dependence between N_i and N_f for different loading conditions. The failure analysis clearly show that the crack initiation occurs long before the final rupture. Nevertheless, although the load conditions and the individual lives are different, the values of the N_i/N_f ratio are very similar.

The maximum normal stress associated with the fatigue crack initiation life N_i and total fatigue life N_f for different stress ratio (R) values is shown in Fig. 6. As can be seen from Fig. 6, for all specimens, the fatigue crack initiation life and the total fatigue life decrease

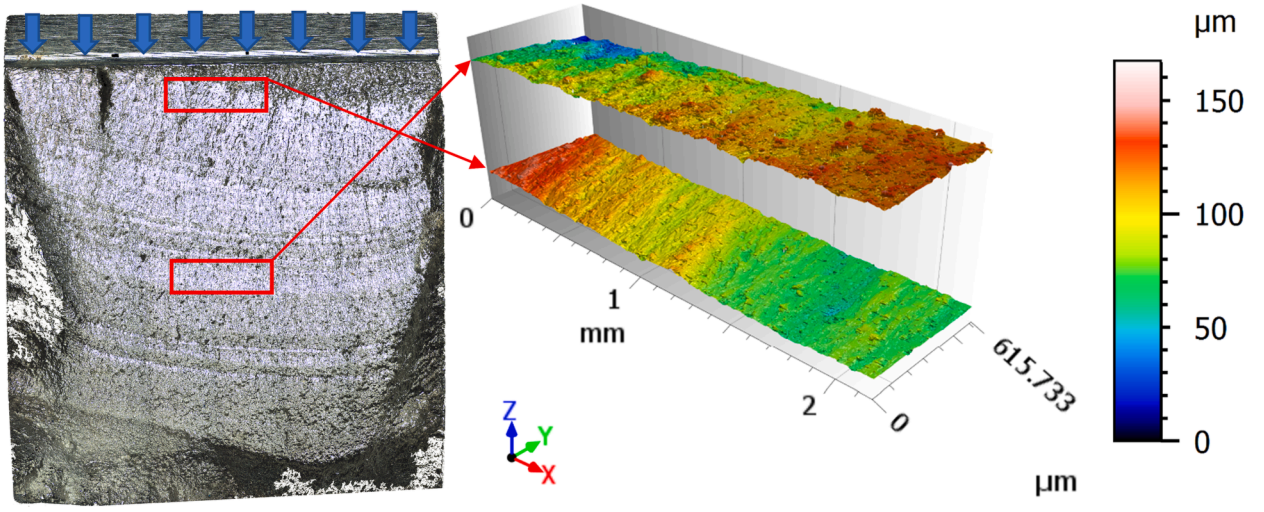

Fig. 12. Three-dimensional fracture surface of the initiation region (at the bottom) and of the propagation region (at the top) for the S7 specimen.

with increasing values of R and maximum normal stress σ_{max}.

3.2. Fracture surface topography parameters

Damage on the fracture surface during the fatigue test, regardless of stress ratio R and acting forces, was intrinsically associated with the tested conditions. According to this assumption, the formed topography of the fracture surface is inherently reflected in the analysis of the fracture surface of the specimen. Fig. 7 shows the fracture surfaces created for the different loading scenarios presented in Table 3. Simultaneous display of fractures surfaces, either in before extracting and composed in the order S1–S7, is also presented. At the bottom, it is also exhibited the corresponding histogram which allows to observe the height distribution with the drawn Firestone curves that represent the cumulating functions of the depth distribution. As can be seen, the curves are rather similar for all cases, which is an interesting outcome. On the other hand, there is a high concentration of data in the middle of the histogram. Fig. 8 shows the extracted surfaces of fractures with the identification of the region of interest (ROI).

Table 5 summarizes the main parameters of the fracture surface measurements, namely *Sx* and *Vx*, computed from the fracture surfaces of the tested specimens. The units for each parameter are shown in the Nomenclature section. The three columns highlighted in green represent the surface topography parameters (*Sq, Sa,* and *Sz*) selected for the analysis and used in discussion.

Fig. 9 plots all measured *Sx* and *Vx* parameters against the *R* values. Overall, the former parameters seem to occupy the same range, irrespective of the stress ratio and the loading conditions. Regarding the latter parameters, the intervals are similar for the lowest and the highest stress ratios but are lower than that of the intermediate *R* value.

3.3. Fractal analysis results

The plots of fractal dimension (coarse and extra-fine resolutions) with coefficients of correlation (R^2) and slopes for two calculated regression lines for extreme D_f values (S3 – minimum, and S4 - maximum) are presented in Fig. 10. Fractal dimension D_f results for all specimens are presented in Appendix A. Fractal dimensions were computed by the EBM and enclosing boxes in real unit method. The results show that both methods give almost identical values. In the case of the analyzed surfaces, the measurement resolution has a greater impact on the results. This is confirmed in the boxplots shown in Fig. 11. For each boxplot, the central mark (red line) indicates the median, and the bottom and top edges of the box indicate the 25th and 75th percentiles, respectively. The whiskers extend to the most extreme data points without considering outliers, and the outliers are plotted individually using the '+' marker symbol.

3.4. Surface morphology of fracture zones

Fig. 12 shows a zoom of the initiation area (lower surface) and the propagation area (upper surface) which allows a better understanding of the pits and valleys distributions for these two particular regions of the S7 specimen (σ_{max} = 349 MPa, and R = -1). Unlike the previous cases, these measurements were carried out using a 100x magnification, a vertical resolution of 6.6 nm and a lateral resolution of 1.46 μm. The grey view (10 × objective) is the original photograph taken by the measurement system after all the images of the fatigue fracture surface have been assembled. Clearly, only a single crack initiated at the notch, and then it propagated to the centre of the specimen, where it can be seen several crack fronts marked on the fracture surface. The local direction of crack propagation near initiation site indicates that crack initiation have started asymmetrically and not at the same time at all sites. However, the entire fracture surface method and their characteristic features are naturally reflected in some of the surface topography

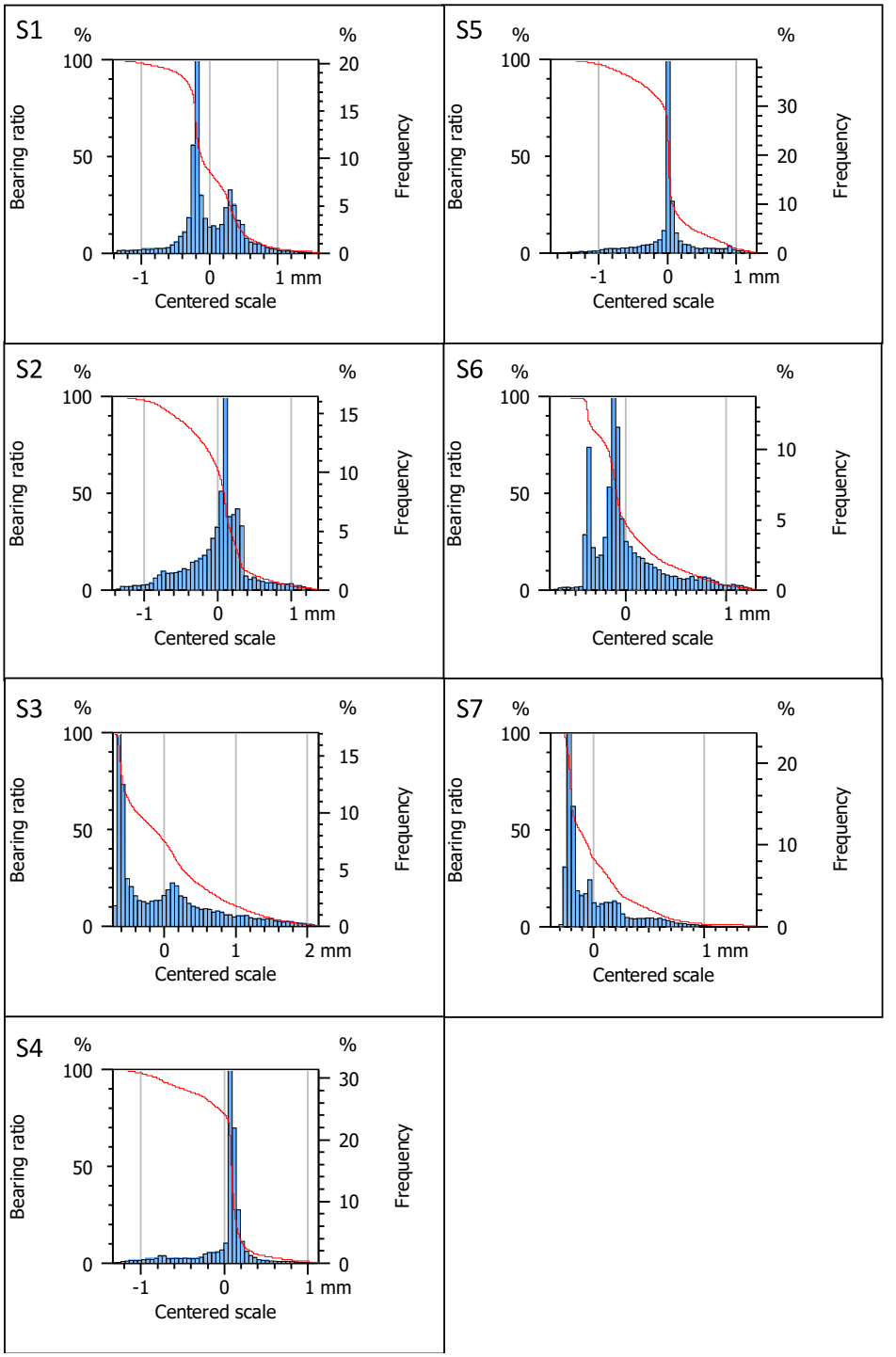

Fig. 13. Abbott-Firestone curves obtained from the height distribution for the centered z-axis coordinate. The vertical axis represents the bearing ratio (%), and the horizontal axis represents the depth (measurement unit).

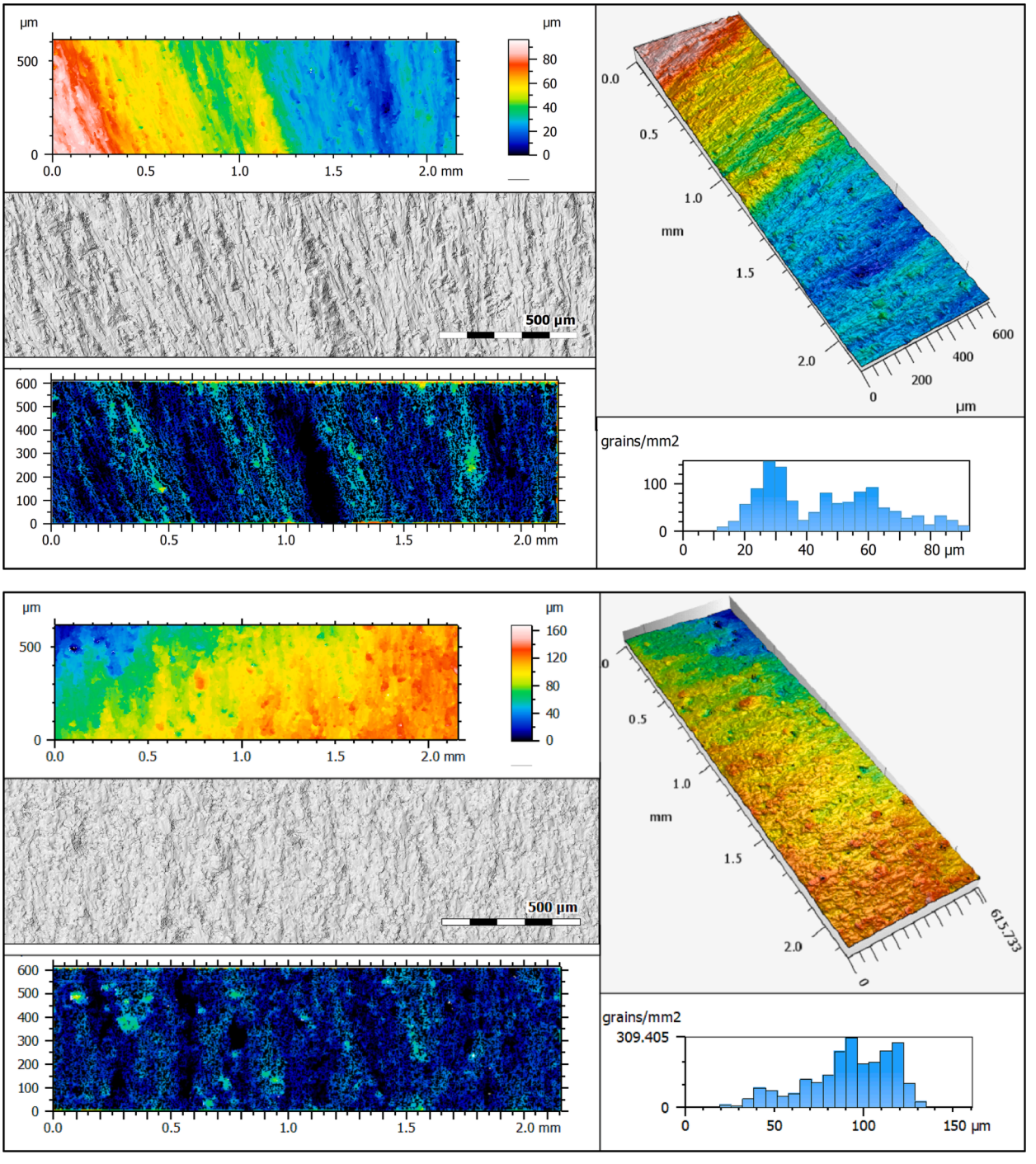

Fig. 14. Visualization of exemplary fracture area with the furrows, and peak count distribution histogram, for: (a) initiation zone; and (b) propagation zone.

Table 6
Results for maximum furrow depth, mean furrow depth, and mean furrow density (specimen S7).

Parameters	Initiation value	Propagation value	Unit
Maximum depth of furrows	54.58	77.19	μm
Mean depth of furrows	9.75	13.71	μm
Mean density of furrows	1122.17	1321.84	cm/cm^2

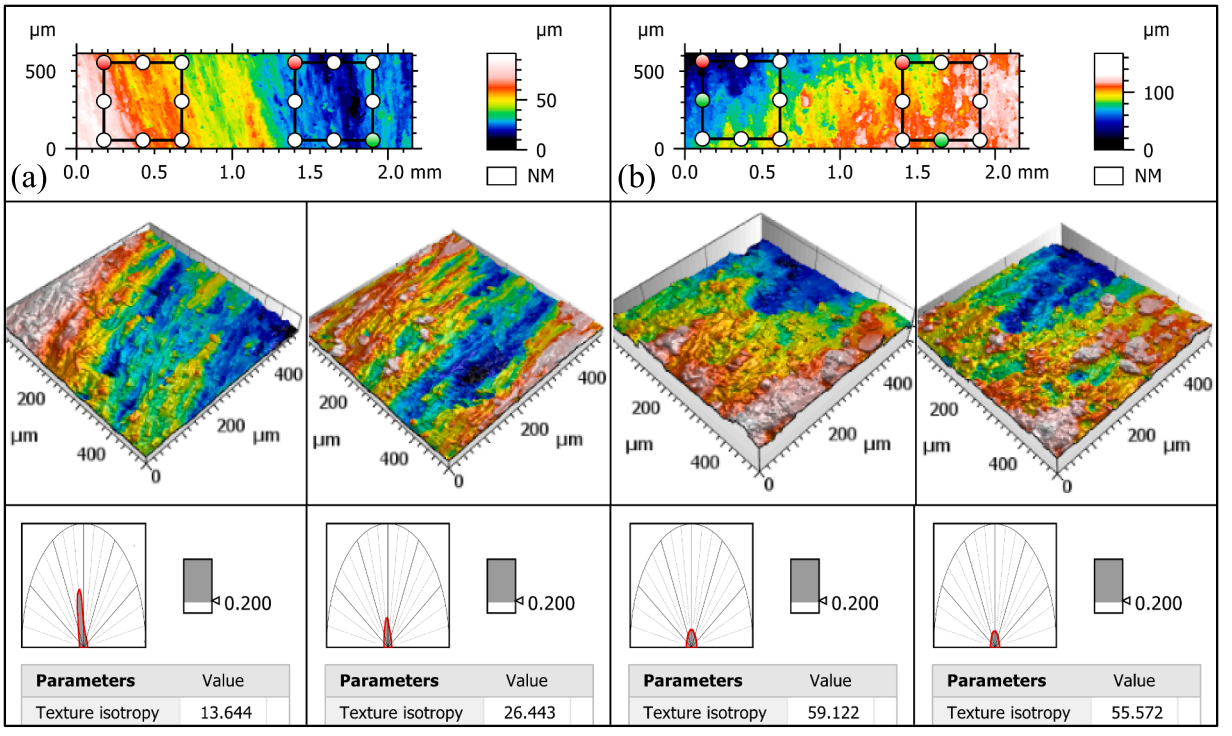

Fig. 15. Visualization of fracture individual zones for the S7 specimen and their texture isotropy values: (a) initiation zone; and (b) propagation zone.

parameters. The same criterion was applied to all specimens. In previous papers the same approach has been successfully applied to other loading conditions, material types, and specimen geometries. In the discussion section, the furrows analysis is presented and the parameters describing the micro-valleys network are determined.

4. Discussion

4.1. Surface topography analysis

The functional analysis in the form of Abbott-Firestone bearing ratio curves and depth distribution histograms (see Fig. 13) was performed with the centered scale. The y-axis represents the height distribution, displayed as a histogram, which gives the probability (frequency) for points to be at a given height. Owing to the random nature of peaks and valleys, the comparison of the respective Abbott–Firestone curves requires a common point of reference for heights. A bin of the histogram is defined by its width (height interval) and its frequency. From a mathematical point of view, Abbott-Firestone curve is the cumulative distribution function of the surface area. Histograms are characterized by one significant peak value that occurs near zero on the centered height scale. This confirms the assumption that the crack propagates symmetrically on both sides of the specimen under cyclic bending loading.

Another clear evidence is that both the fatigue crack initiation area and the fatigue crack propagation area change considerably with the loading case. These differences can be distinguished in Fig. 14 which shows the S7 specimen.

($\sigma_{max} = 349$ MPa, and $R = -1$). In the initiation zone (see Fig. 14(a)), the valley distribution is less uniform than for the case of the propagation zone (see Fig. 14(b)). At the surface of crack initiation, the furrows are shallower and there is an evident directionality of the furrows. Furthermore, the results of Table 6 clearly indicate that the values of the maximum depth of furrows are smaller in the initiation zone than in the propagation zone. These values expressed in percentage, correspond to 70.7% for the maximum depth of furrows, 71.1% for the mean depth of furrows, and 84.9% for the mean density of furrows.

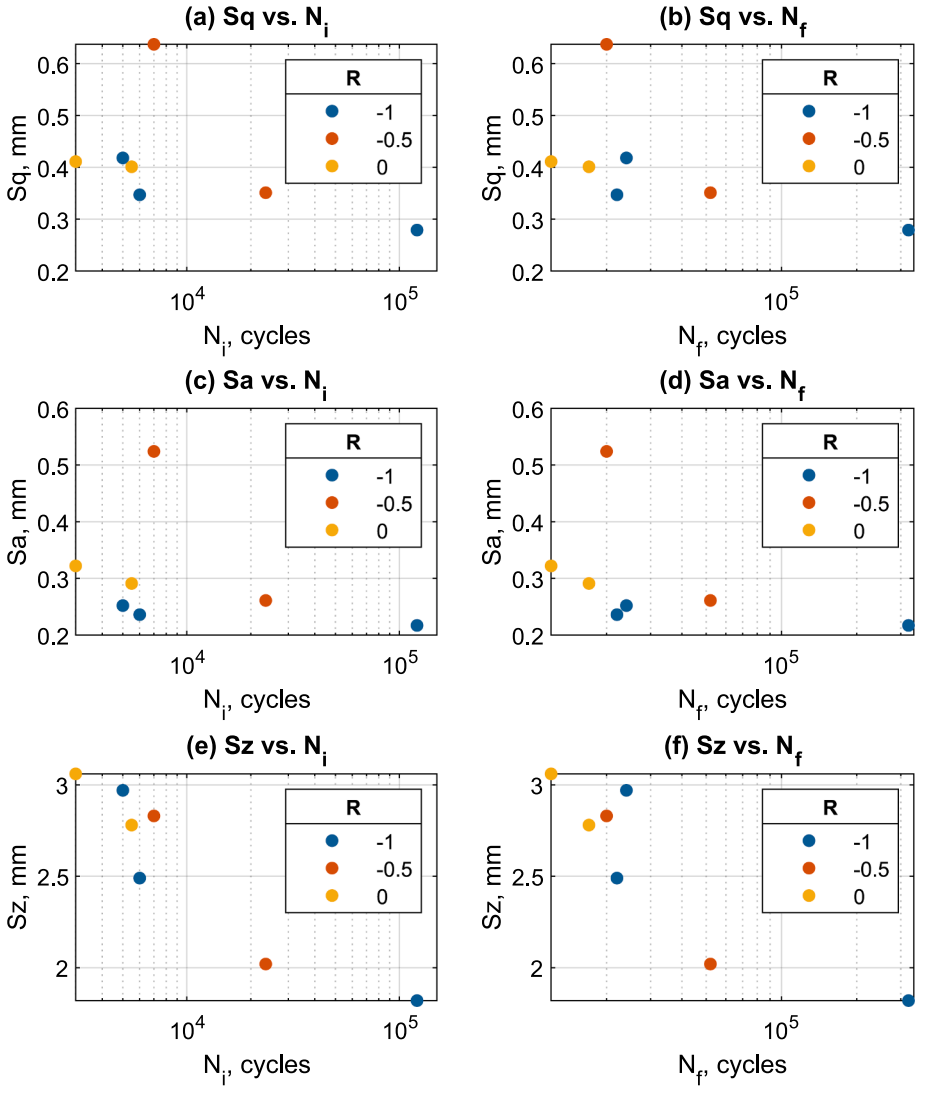

Fig. 16. Fracture surface topography parameters versus: N_i (a, c, e); and N_f (b, d, f).

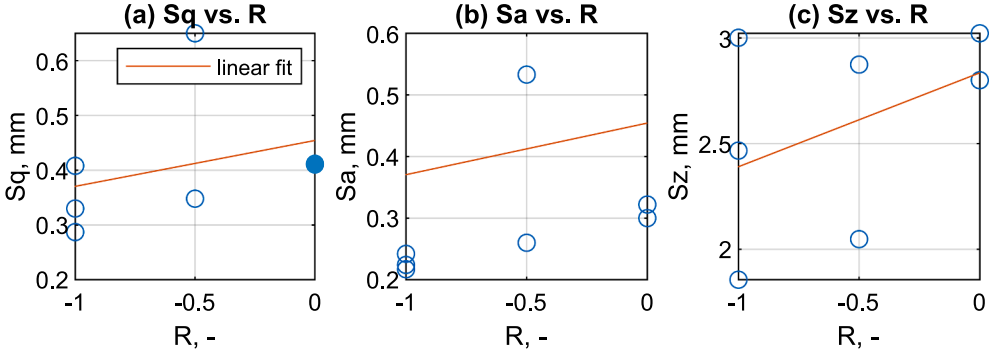

Fig. 17. Fracture surface topography parameters versus stress ratio R.

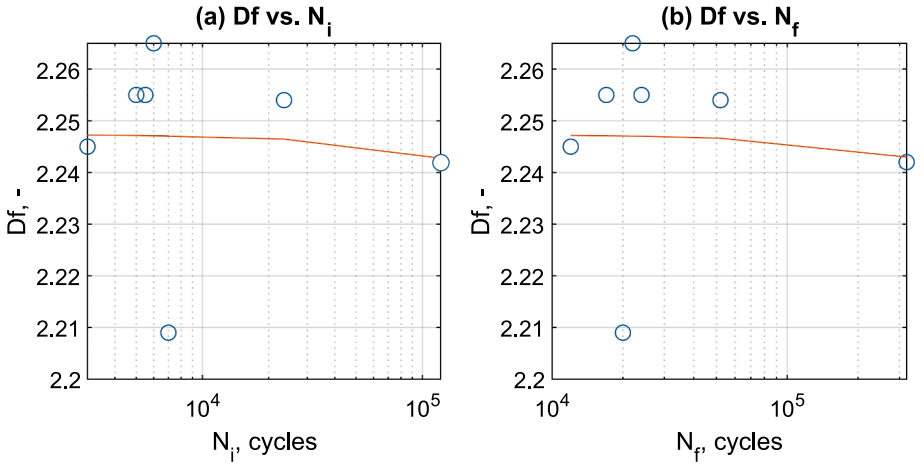

Fig. 18. Fractal dimension D_f versus: (a) N_i; and (b) N_f.

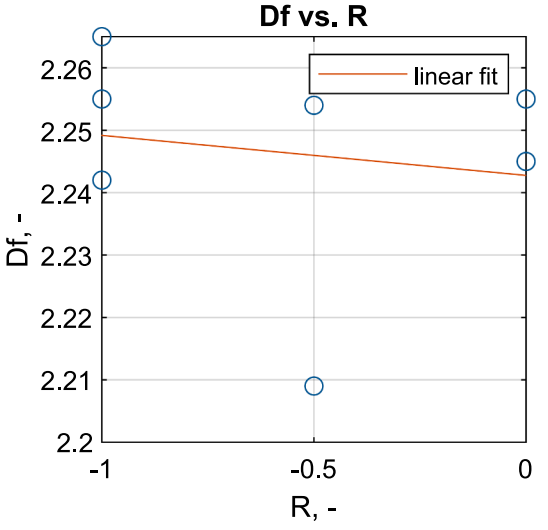

Fig. 19. Fractal dimension D_f versus stress ratio R.

The distribution of the peak heights with the maximum number of peaks per square millimeter can also be seen in Fig. 14 in the form of peak count distribution histograms. Both parameters take higher values for the propagation zone. In addition, the maximum number of peaks per square millimeter is higher for the propagation zone (almost 310), while for the initiation zone, it is below 150. The maximum peak values are also greater for the propagation zone, around 160 μm, while in the initiation zone, it is about 90 μm.

Surface roughness is the result of the simultaneous interaction of several independent factors, both random and determined. Consequently, it has a very complex microgeometry. There are evident differences between the various individual fracture zones, as exhibited in Fig. 15. For the purposes of this analysis, these two additional individual zones allow a better awareness of such complexity. It is clear that the directivity of the geometric structure depends on the fracture zone and it results from the kinematics of the fracture process.

The isotropy of a medium is generally based on the fact that it exhibits the same physical or geometric properties in all directions. The isotropy of a surface, therefore, means that the surface has the same structure in all directions. It is also a perfectly symmetrical structure with respect to all possible axes of symmetry. In the examined case, the isotropy was determined by analyzing the auto-correlation function. The shape of this function for anisotropic surfaces is asymmetric, slender and elongated in one direction, which was found for the initiation zone (see Fig. 15(a)). The isotropy value, in this case, was relatively low, approximately equal to 14% or 26%. On the other hand, isotropic surfaces are characterized by the circular and symmetrical functions which was observed in the propagation zone, where the isotropy value was about 56% or 59% (see Fig. 15(b)).

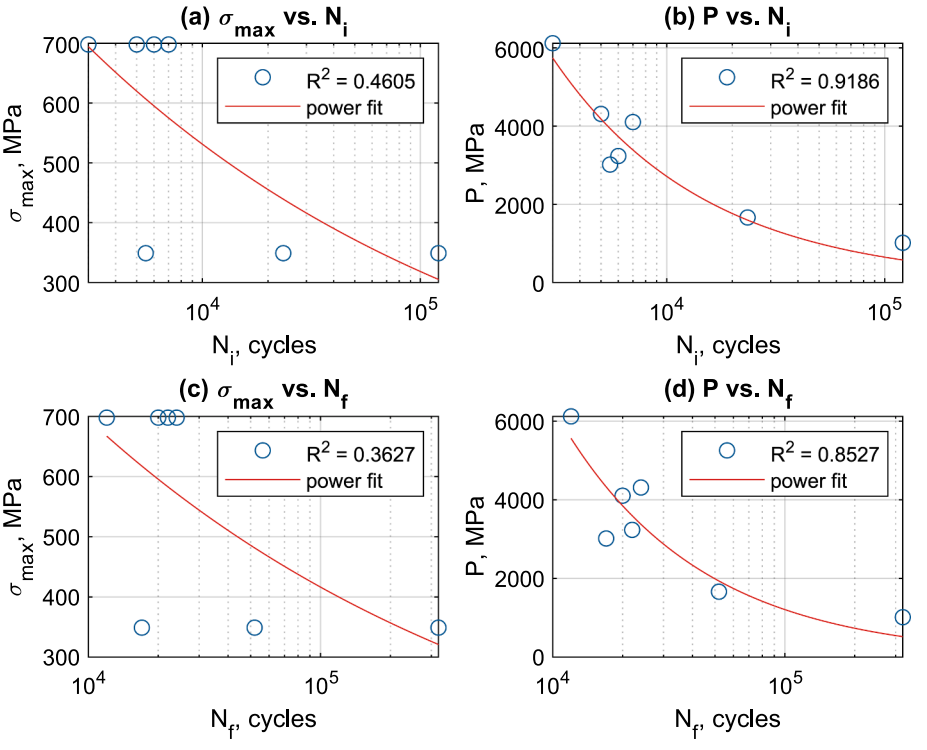

Fig. 20. Power fit relationship between: (a) maximum bending stress σ_{max} versus N_i; (b) topographic stress factor P versus N_i; (c) maximum bending stress σ_{max} versus N_f; and (d) topographic stress factor P versus N_f.

4.2. Fatigue life assessment

The results of the fracture surface topography parameters presented in Section 3.2 showed that the values of *Sq*, *Sa*, and *Sz* do not show satisfactory consistency to obtain linear functions for all the tested samples. This situation is even more clear in Figs. 16 and 17. The former plots the above-mentioned parameters against the fatigue crack initiation life N_i, and the total fatigue life N_f, while the latter plots the above-mentioned parameters against the stress ratio R.

As for the standard parameters of surface topography (*Sx, Vx*), the same conclusions were drawn with respect to the fractal dimension D_f, see Figs. 18 and 19. The former displays the correlation between the fractal dimension D_f and both the fatigue crack initiation life N_i and the total fatigue life N_f, while the latter displays the correlation between the fractal dimension D_f and the stress ratio R. In the two figures the fractal dimension D_f was calculated in real units with fine resolution which was found to be the most appropriate. Nevertheless, the results also do not show satisfactory consistency to obtain linear functions for all tested samples.

Therefore, in order to overcome this issue, it is proposed a combination of the most suitable surface topography parameters along with other fatigue quantities (e.g. fatigue crack initiation life N_i) to develop a suitable approach to assess the fatigue lifetime. The proposed parameter encompassed the fractographic fracture surface state and the stress state and can be written as follows:

$$P = \frac{Sq}{Sa} \times (D_f + R) \times \sigma_{max}(\text{MPa})$$

where *Sq* and *Sa* are surface topography parameters, D_f is the fractal dimension, R is the stress ratio, and $\sigma_{max}$is the maximum bending stress. P parameter aims to reflect three elements: fracture surface topography ($\frac{Sq}{Sa}$); stress ratio modulated by the fractal dimension $(D_f + R)$; and the maximum bending stress σ_{max}, respectively.

Fig. 20 presents the relationship between the maximum bending stress σ_{max} and the fatigue crack initiation life N_i (Fig. 20 (a)) and the total life N_f (Fig. 20(c)); as well as the relationship between the topographic stress factor P and the fatigue crack initiation life N_i (Fig. 20 (b)) and the total life N_f (Fig. 20(d)). Through the analysis of the coefficient of determination R^2, it is possible to conclude that the proposed P parameter fits better the data than the classical maximum bending stress σ_{max}.

Additional statistical analysis for fatigue data was performed. The main results are presented in Fig. 21 and Table 7. Linear fit correlated well with the results of the P parameter. It should be noted that all of the tested cases results fell in 1.3 scatter bands, while the analysis conducted using the maximum bending stress σ_{max} led to results within 1.7 scatter bands.

The measured fatigue crack initiation life N_i and the fitted fatigue crack initiation life N_{ical} computed through the proposed topographic stress factor P (see Eq. (4)) are compared in are compared in Fig. 22. As can be seen, the calculations correlate well with the experimental results since all of the tested cases results fall in a factor-of-two scatter bands. In a similar way, regarding the total

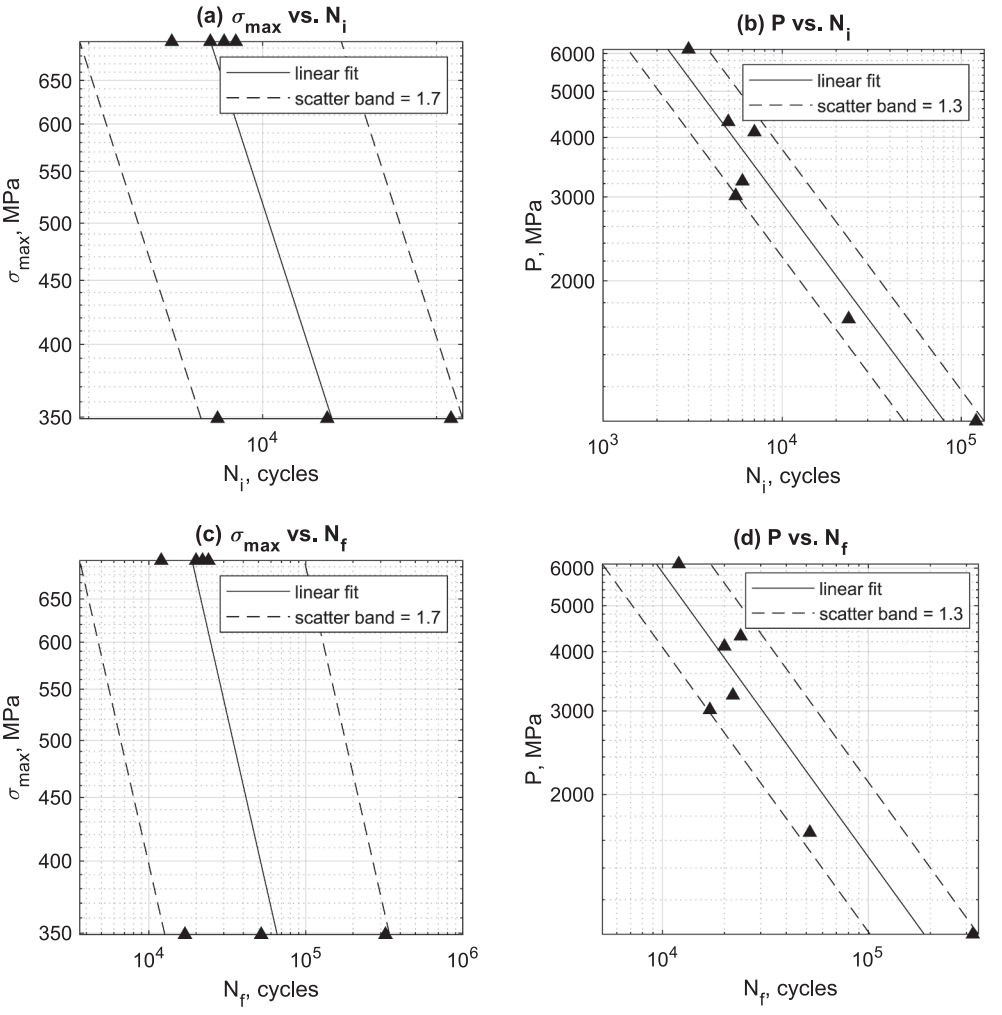

Fig. 21. Linear fit relationship between: (a) maximum bending stress σ_{max} and N_i; (b) topographic stress factor P and N_i; (c) maximum bending stress σ_{max} and N_f; and (d) topographic stress factor P and N_f.

Table 7
Statistical analysis of linearized stress-life (σ_{max}-N) and topographic stress factor-Life (P-N) fatigue data.

Parameters	σ_{max}-N_i	P-N_i	σ_{max}-N_f	P-N_f
Variance (Estimate)	0.1958	0.0295	0.1772	0.0410
Standard Deviation (Estimate)	0.4425	0.1719	0.4210	0.2024

fatigue life, Fig. 22 shows that both the measured total fatigue life N_f and the fitted total fatigue life N_{ical} computed through the proposed topographic stress factor P (see Eq. (5)) are in good agreement, with all data points within factor-of-two scatter bands.

$N_{ical} = 7 \times 10^{10} \times P^{-1.977}$; (4)

$N_{fcal} = 2 \times 10^{10} \times P^{-1.668}$. (5)

5. Concluding remarks

A post-mortem fractography analysis was conducted for 2017-T4 aluminium alloy subjected to cyclic bending. A comparative analysis of fracture surface features was carried out using standard surface topography parameters (such as, root mean square height *Sq*, arithmetical mean height *Sa*, maximum height *Sz*) and non-standard surface topography parameters (such as, fractal dimension D_f).

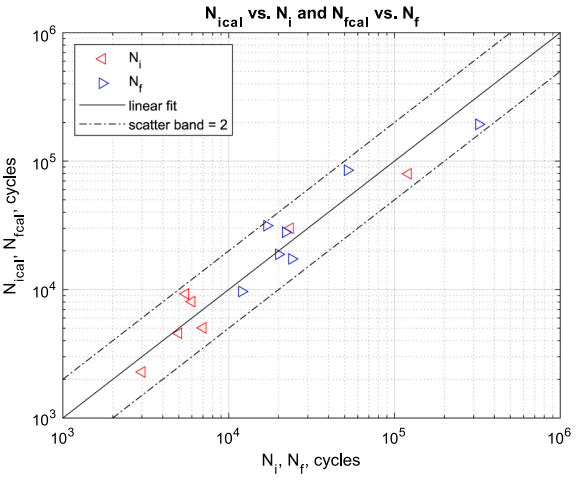

Fig. 22. Experimental fatigue crack initiation life (N_i) versus calculated fatigue crack initiation life (N_{ical}) and experimental total fatigue life (N_f) versus calculated total fatigue life (N_{fcal}).

A damage parameter combining both the fractographic characteristics and the stress state was introduced to assess the fatigue durability. The following conclusions can be drawn:

- The crack initiation occured long before the final fracture. Although the load conditions and the individual lives were different, the values of the N_i/N_f ratio were very similar.
- The initiation zone exhibited the typical properties of anisotropic surfaces, while the surfaces of propagation zones were isotropic;
- the classical maximum bending stress did not reveal satisfactory correlation to be a reliable fatigue damage quantifier in terms of fatigue crack initiation life or total fatigue life;
- The topographic stress factor P led to high coefficient of determination R^2 which suggests that it can be used for fatigue life assessment in the context of post-mortem elements subjected to cyclic bending;
- the fractal analysis based on the enclosing boxes method (EBM) is more accurate when it is used an extra-fine resolution.

Future research should focus on the broad data mining by utilizing other tested materials and loading scenarios via the introduction of data-driven approaches. Entire fracture surface method has universal application, allowing the analysis of a wide range of engineering problems encompassing different tested materials, geometric configurations and loading histories. A limitation in the use of this method is the need for an interpretation for the use of the "entire" area of fracture surface relative to large dimensions or irregular shapes. In the cases addressed before, there have been no extensive discontinuities, large faults or disqualifying material discontinuities. Therefore, in the future, research using this method should also focus on damage in more geometrically complex elements. Due to the universality of surface metrological values, it is possible to adapt these methods to describe fatigue cracking processes in other material groups, such as non-metals.

Declaration of Competing Interest

The authors declare that they have no known competing financial interests or personal relationships that could have appeared to influence the work reported in this paper.

Data availability

Data will be made available on request.

Appendix A. . Fractal dimension D_f results

The plots of fractal dimension (coarse and extra-fine resolutions) with coefficients of correlation (R^2) and slopes for two calculated regression lines are presented in Fig. A1.

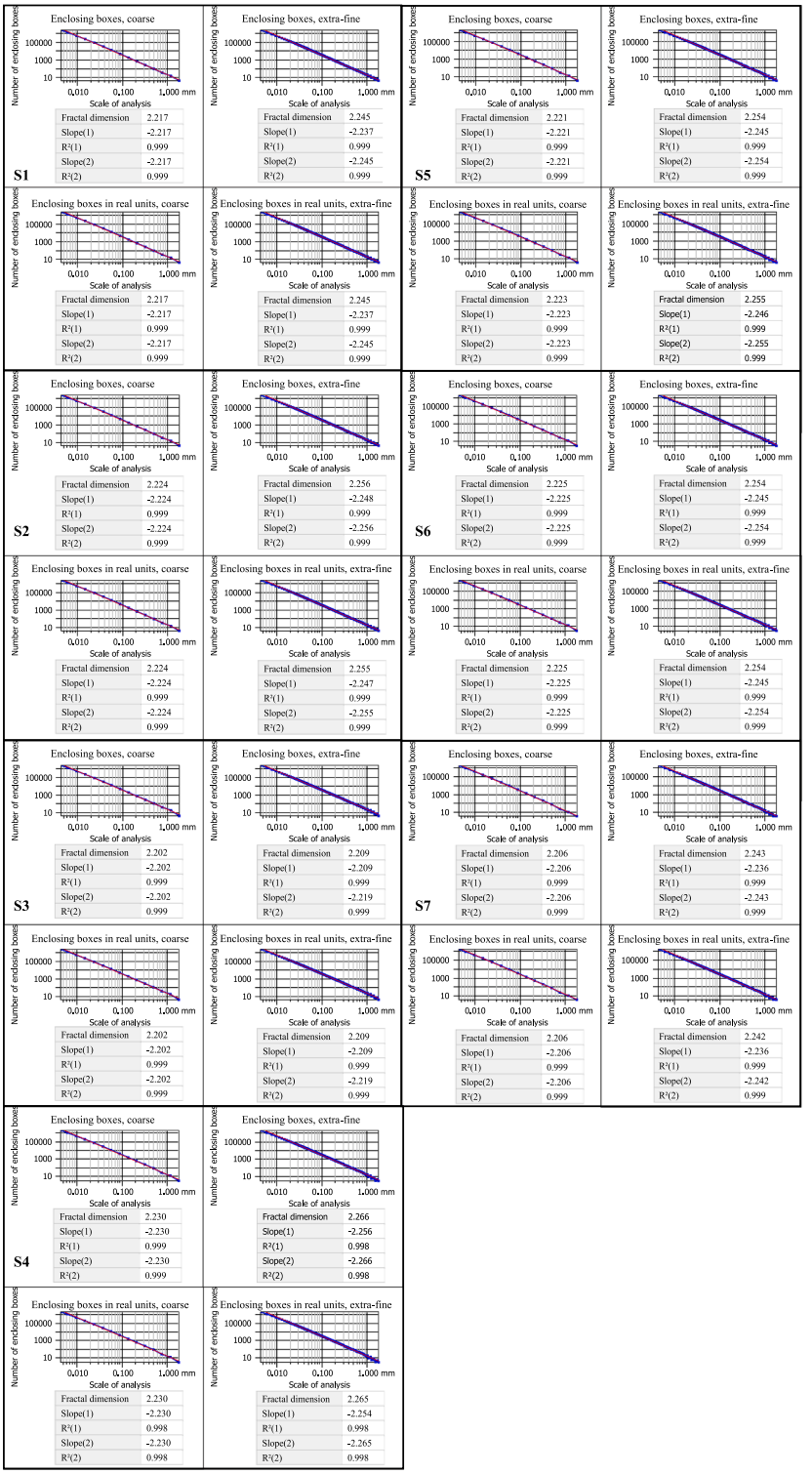

Fig. A1. Fractal dimension D_f results.

References

[1] D. Rozumek, S. Faszynka, Surface cracks growth in aluminum alloy AW-2017A-T4 under combined loadings, Eng. Fract. Mech. 226 (2020), 106896, https://doi.org/10.1016/J.ENGFRACMECH.2020.106896.

[2] S.P. Zhu, Y. Ai, D. Liao, J.A.F.O. Correia, A.M.P. De Jesus, Q. Wang, Recent advances on size effect in metal fatigue under defects: a review, Int. J. Fract. 234 (1) (2021) 21–43, https://doi.org/10.1007/S10704-021-00526-X.
[3] M. Brunet, B. Malard, N. Ratel-Ramond, C. Deshayes, S. Joulié, B. Warot-Fonrose, P. Sciau, J. Douin, F. de Geuser, A. Deschamps, Precipitation in original Duralumin A-U4G versus modern 2017A alloy, Materialia (Oxf). 8 (2019), 100429, https://doi.org/10.1016/j.mtla.2019.100429.
[4] R. Branco, J.D. Costa, L.P. Borrego, W. Macek, F. Berto, Notch fatigue analysis and life assessment using an energy field intensity approach in 7050–T6 aluminium alloy under bending-torsion loading, Int. J. Fatigue. 162 (2022), 106947, https://doi.org/10.1016/J.IJFATIGUE.2022.106947.
[5] D. Rozumek, J. Lewandowski, G. Lesiuk, Z. Marciniak, J.A. Correia, W. Macek, The energy approach to fatigue crack growth of S355 steel welded specimens subjected to bending, Theor. Appl. Fract. Mech. 121 (2022), 103470, https://doi.org/10.1016/J.TAFMEC.2022.103470.
[6] W. Macek, A. Tomczyk, R. Branco, M. Dobrzyński, A. Seweryn, Fractographical quantitative analysis of EN-AW 2024 aluminum alloy after creep pre-strain and LCF loading, Eng Fract Mech (2023) 109182, https://doi.org/10.1016/J.ENGFRACMECH.2023.109182.
[7] R. Masoudi Nejad, N. Sina, D. Ghahremani Moghadam, R. Branco, W. Macek, F. Berto, Artificial neural network based fatigue life assessment of friction stir welding AA2024-T351 aluminum alloy and multi-objective optimization of welding parameters, Int. J. Fatigue. 160 (2022), 106840, https://doi.org/10.1016/J.IJFATIGUE.2022.106840.
[8] A. Janeczek, J. Tomków, D. Fydrych, The Influence of Tool Shape and Process Parameters on the Mechanical Properties of AW-3004 Aluminium Alloy Friction Stir Welded Joints, Materials 14 (2021) 3244, https://doi.org/10.3390/MA14123244.
[9] S. Vantadori, J. Vázquez Valeo, A. Zanichelli, A. Carpinteri, R. Luciano, Structural integrity of shot peened Ti6Al4V specimens under fretting fatigue, Int. J. Fract. 234 (2021) 45–55, https://doi.org/10.1007/S10704-021-00523-0/FIGURES/10.
[10] W. Macek, Ł. Pejkowski, R. Branco, R. Masoudi Nejad, K. Żak, Fatigue fracture surface metrology of thin-walled tubular austenitic steel specimens after asynchronous loadings, Eng. Fail Anal. 138 (2022), 106354, https://doi.org/10.1016/J.ENGFAILANAL.2022.106354.
[11] W. Macek, G. Robak, K. Żak, R. Branco, Fracture surface topography investigation and fatigue life assessment of notched austenitic steel specimens, Eng. Fail Anal. 135 (2022), 106121, https://doi.org/10.1016/J.ENGFAILANAL.2022.106121.
[12] R. Branco, J.D. Costa, L.P. Borrego, F. Berto, S.M.J. Razavi, W. Macek, Comparison of different one-parameter damage laws and local stress-strain approaches in multiaxial fatigue life assessment of notched components, Int. J. Fatigue. 151 (2021), 106405, https://doi.org/10.1016/J.IJFATIGUE.2021.106405.
[13] Z. Marciniak, R. Branco, R.F. Martins, W. Macek, D. Rozumek, Non-local volumetric approach to analysis defect's shape influence on specimens durability subjected to bending and torsion, Int. J. Fatigue 167 (2023), 107317, https://doi.org/10.1016/J.IJFATIGUE.2022.107317.
[14] Q.Y. Deng, S.P. Zhu, X. Niu, G. Lesiuk, W. Macek, Q. Wang, Load path sensitivity and multiaxial fatigue life prediction of metals under non-proportional loadings, Int. J. Fatigue. 166 (2023), 107281, https://doi.org/10.1016/J.IJFATIGUE.2022.107281.
[15] K. Aliakbari, R.M. Nejad, S.K.P. Toroq, W. Macek, R. Branco, Assessment of unusual failure in crankshaft of heavy-duty truck engine, Eng. Fail Anal. 134 (2022), 106085, https://doi.org/10.1016/J.ENGFAILANAL.2022.106085.
[16] S. Natarajan, E.T. Ooi, C. Birk, C. Song, Adaptive modelling of dynamic brittle fracture - a combined phase field regularized cohesive zone model and scaled boundary finite element approach, Int. J. Fract. 2022 (2022) 1–22, https://doi.org/10.1007/S10704-022-00634-2.
[17] S. Duda, M. Smolnicki, T. Osiecki, G. Lesiuk, Determination of fracture energy (mode I) in the inverse fiber metal laminates using experimental–numerical approach, Int. J. Fract. 234 (2021) 213–222, https://doi.org/10.1007/S10704-021-00566-3/FIGURES/12.
[18] M. Duda, D. Rozumek, G. Lesiuk, M. Smolnicki, B. Babiarczuk, J. Warycha, Fatigue crack growth under mixed-mode I + II and I + III in heat treated 42CrMo4 steel, Int. J. Fract. 234 (2021) 235–248, https://doi.org/10.1007/S10704-021-00585-0/FIGURES/18.
[19] C. Santus, L. Romanelli, T. Grossi, P. Neri, L. Romoli, A.H.A. Lutey, M. Pedranz, M. Benedetti, Torsional-loaded notched specimen fatigue strength prediction based on mode I and mode III critical distances and fracture surface investigations with a 3D optical profilometer, Int. J. Fatigue. 161 (2022), 106913, https://doi.org/10.1016/J.IJFATIGUE.2022.106913.
[20] W. Macek, D. Rozumek, G.M. Królczyk, Surface topography analysis based on fatigue fractures obtained with bending of the 2017A–T4 alloy, Measurement (Lond). 152 (2020), 107347, https://doi.org/10.1016/j.measurement.2019.107347.
[21] International Organisation of Standardization, ISO 25178, Geometric Product Specifications (GPS) – Surface Texture: Areal, 2010.
[22] P. Podulka, W. Macek, R. Branco, R.M. Nejad, Reduction in Errors in Roughness Evaluation with an Accurate Definition of the S-L Surface, Materials 16 (2023) 1865, https://doi.org/10.3390/MA16051865.
[23] B.B. Mandelbrot, E. Dann, A.J.P. Passoja, Fractal character of fracture surfaces of metals, Nature. 308 (1984) 721–722, https://doi.org/10.1038/308721a0.
[24] E. Bouchaud, G. Lapasset, J. Planès, Fractal dimension of fractured surfaces: a universal value? Europhys. Lett. 13 (1990) 73, https://doi.org/10.1209/0295-5075/13/1/013.
[25] W. Macek, R. Branco, M. Korpyś, T. Łagoda, Fractal dimension for bending–torsion fatigue fracture characterisation, Measurement. 184 (2021), 109910, https://doi.org/10.1016/J.MEASUREMENT.2021.109910.
[26] H. Lauschmann, K. Tesař, K. Jiroušková, Quantitative fractography of fatigue cracks: a new solution in 3D, Proc. Struct. Integr. 23 (2019) 107–112, https://doi.org/10.1016/J.PROSTR.2020.01.071.
[27] W. Macek, R. Masoudi Nejad, S.-P. Zhu, J. Trembacz, R. Branco, J.D.M. Costa, J.A.M. Fereira, C. Capela, Effect of bending-torsion on fracture and fatigue life for 18Ni300 steel specimens produced by SLM, Mech. Mater. 178 (2023) 104576, https://doi.org/10.1016/J.MECHMAT.2023.104576.
[28] I.J. Wietecha-Reiman, A. Segall, X. Zhao, T.A. Palmer, Combining fractal and topological analyses to quantify fracture surfaces in additively manufactured Ti-6Al-4V, Int. J. Fatigue. (2022), 107232, https://doi.org/10.1016/J.IJFATIGUE.2022.107232.
[29] K. Slámečka, P. Ponížil, J. Pokluda, Quantitative fractography in bending-torsion fatigue, Mater. Sci. Eng. A. 462 (2007), https://doi.org/10.1016/j.msea.2006.03.153.
[30] L. Konate, D. Kondo, L. Ponson, Numerical fracture mechanics based prediction for the roughening of brittle cracks in 2D disordered solids, Int. J. Fract. 230 (2021) 225–240, https://doi.org/10.1007/S10704-021-00576-1/FIGURES/10.
[31] E. Berthier, A. Mayya, L. Ponson, Damage spreading in quasi-brittle disordered solids: II. What the statistics of precursors teach us about compressive failure, J. Mech. Phys. Solids. 162 (2022), 104826, https://doi.org/10.1016/J.JMPS.2022.104826.
[32] Y.G. Cao, S.H. Zhang, K. Tanaka, Calculation method for maximum low-cycle fatigue loads using FRASTA reconstruction data, Int. J. Fract. (2013), https://doi.org/10.1007/s10704-013-9862-z.
[33] T. Kobayashi, D.A. Shockey, The relationship between fracture surface roughness and fatigue load parameters, Int. J. Fatigue. 23 (2001) 135–142, https://doi.org/10.1016/S0142-1123(01)00149-9.
[34] W. Macek, D. Sampath, Ł. Pejkowski, K. Żak, A brief note on monotonic and fatigue fracture events investigation of thin-walled tubular austenitic steel specimens via fracture surface topography analysis (FRASTA), Eng. Fail Anal. 134 (2022), 106048, https://doi.org/10.1016/J.ENGFAILANAL.2022.106048.
[35] K. Leksycki, J.B. Królczyk, Comparative assessment of the surface topography for different optical profilometry techniques after dry turning of Ti6Al4V titanium alloy, Measurement. 169 (2021), 108378, https://doi.org/10.1016/J.MEASUREMENT.2020.108378.
[36] S. Catalucci, A. Thompson, S. Piano, D.T. Branson, R. Leach, Optical metrology for digital manufacturing: a review, Int. J. Adv. Manuf. Technol. 120 (2022) 4271–4290, https://doi.org/10.1007/S00170-022-09084-5/FIGURES/10.
[37] W. Macek, Fracture surface formation of notched 2017A–T4 aluminium alloy under bending fatigue, Int. J. Fract. 234 (2021) 141–157, https://doi.org/10.1007/S10704-021-00579-Y/FIGURES/16.
[38] W. Macek, The impact of surface slope and calculation resolution on the fractal dimension for fractures of steels after bending-torsion fatigue, Surf. Topogr. 10 (2022), 015030, https://doi.org/10.1088/2051-672X/AC58AE.
[39] W. Macek, Post-failure fracture surface analysis of notched steel specimens after bending-torsion fatigue, Eng Fail Anal. (2019), https://doi.org/10.1016/j.engfailanal.2019.07.056.
[40] A. Thum, Verformung, Spannung und Kerbwirkung Eine Einf, VDI-Verl, Düsseldorf, 1960.